Materials Advances

Accepted Manuscript

This article can be cited before page numbers have been issued, to do this please use: S. Merazga, Y. Chelali, F. Mohamed, A. Moreno-Zuria and M. Mohamedi, *Mater. Adv.*, 2026, DOI: 10.1039/D6MA00390G.

ROYAL SOCIETY OF CHEMISTRY

rsc.li/materials-advances

View Article Online
DOI: 10.1039/D6MA00390G

Optimizing Silver Incorporation in MnO_x Air Cathodes to Balance Power Density and Cycling Stability in Rechargeable Zn–Air Batteries

Saloua Merazga,[1,2] Yahia Chelali,[1] Fatahine Mohamed,[1] Alonso Moreno Zuria[1] and Mohamed Mohamedi[1*]

[1]Institut National de la Recherche Scientifique (INRS)-Énergie, Matériaux et Télécommunications (EMT), 1650 Boulevard Lionel Boulet, Varennes, Québec, J3X 1P7, Canada. Email: Mohamed.Mohamedi@inrs.ca

[2]Centre de Recherche en Technologie des Semi-Conducteurs pour l'Énergétique (CRTSE), Bd Frantz Fanon, P.O. Box 140, Alger-7 Merveilles, Algiers DZ-16038, Algeria.

Abstract

Rechargeable Zn–air batteries (ZABs) require air cathodes that simultaneously deliver high power output and durable bifunctional oxygen electrocatalysis. Herein, we systematically investigate the effect of controlled Ag incorporation into MnO_x catalysts supported on carbon paper (CP) to elucidate the interplay between conductivity, catalytic reversibility, and long-term stability. Three binderless electrodes CP/MnO_x, CP/$MnO_xAg_{0.03}$, and CP/$MnO_xAg_{0.05}$ were evaluated through polarization, power density, galvanostatic cycling (300 cycles at 2 mA cm^{-2}), and electrochemical impedance spectroscopy (EIS) before and after cycling. Increasing Ag loading significantly enhances electronic conductivity and charge-transfer kinetics, leading to improved instantaneous performance, with CP/$MnO_xAg_{0.05}$ delivering the highest current density (80.5 mA cm^{-2}) and power density (39.1 mW cm^{-2}). However, long-term cycling reveals a distinct optimum at moderate Ag loading. CP/$MnO_xAg_{0.03}$ exhibits the lowest voltage gap (1.09 V) and highest round-trip efficiency (50.6%) after 300 cycles, outperforming both pristine MnO_x and the CP/$MnO_xAg_{0.05}$ electrode. EIS shows that while higher Ag content stabilizes interfacial conductivity, excessive Ag disrupts the balance between oxygen reduction and evolution reactions, resulting in increased polarization growth during cycling. In contrast, moderate Ag incorporation preserves Mn redox-active sites and maintains more symmetric ORR/OER kinetics, ensuring superior bifunctional reversibility and durability. These results demonstrate that maximizing peak power density does not necessarily yield optimal rechargeable performance; instead, achieving a balanced synergy between conductive additives and redox-active oxide centers is critical. This work establishes a

View Article Online
DOI: 10.1039/D6MA00390G

composition-dependent design strategy for bifunctional air cathodes, highlighting optimal Ag loading as a key parameter for developing efficient and durable rechargeable Zn–air batteries.

View Article Online
DOI: 10.1039/D6MA00390G

1. Introduction

Amid the ongoing pursuit of safer and higher-performance energy storage technologies, metal–air batteries (MABs) have attracted significant interest as next-generation energy storage systems because they couple a metallic anode with oxygen from ambient air, enabling very high theoretical energy densities while minimizing the amount of active material stored within the cell.[1-2] First, the use of oxygen from the environment reduces cell weight and increases gravimetric energy density compared with conventional closed systems such as Li-ion batteries. Second, many metal anodes used in these systems (e.g., Zn, Fe, Al, Mg, Na) are earth-abundant, low-cost, and relatively safe, making them attractive for large-scale and sustainable energy storage. Third, MABs often exhibit high theoretical capacities and are compatible with aqueous or solid electrolytes.[3] These features make them particularly appealing for applications ranging from portable electronics to grid-level storage.

Despite the diversity of metal anodes, all MABs share a common electrochemical operating principle based on oxygen electrochemistry at the air electrode. During discharge, the metal anode is oxidized, releasing electrons and metal cations. Simultaneously, oxygen from air is reduced at the cathode via the oxygen reduction reaction (ORR). The overall discharge reaction therefore corresponds to the oxidation of the metal coupled with ORR to form a metal oxide, hydroxide, or peroxide. During charging, the reverse process occurs: the oxygen evolution reaction (OER) regenerates O_2 at the air electrode while the metal species are reduced and redeposited at the anode. Hence, the fundamental mechanism common to all MABs is the coupling of metal oxidation/reduction at the anode with the reversible ORR/OER oxygen electrocatalysis at the air cathode.[4]

Despite notable advances, several critical challenges still hinder the large-scale commercialization of rechargeable MABs. Sluggish ORR and OER kinetics at the air electrode lead to large polarization losses and low round-trip efficiency.[5-6] The development of efficient and durable bifunctional electrocatalysts remains difficult, as many materials suffer from activity degradation and limited long-term stability under cycling conditions.[7] In addition, the air electrode itself can undergo carbon corrosion, catalyst detachment, and pore structure degradation at high anodic potentials, further limiting durability.[8] On the anode side, non-uniform metal plating/stripping often induces dendrite formation, corrosion, and passivation, resulting in poor reversibility and shortened cycle life.[9] Electrolyte-related issues, such as carbonate formation due

View Article Online
DOI: 10.1039/D6MA00390G

to CO_2 absorption in alkaline media and other parasitic reactions, also reduce ionic conductivity and clog the porous cathode structure.[10]

In recent years, the integration of noble metals, including Ru, Pd, Rh, Os, Ir, Ag, Au, and Pt into MnO_2 matrices has been extensively investigated as an effective strategy to improve their inherently low electronic conductivity.[11-12] Among these elements, Ag is particularly notable as a soft, lustrous transition metal possessing remarkably high electrical conductivity and optical reflectivity compared with most metals.[13] In addition, its relatively lower cost among noble metals makes Ag especially attractive for scalable electrochemical technologies. Accordingly, Ag was chosen as a dopant for MnO_2, given its proven capacity to simultaneously improve charge transport and promote the catalytic activity of MnO_2 systems. Pristine MnO_2 typically suffers from poor electrical conductivity and moderate intrinsic activity toward oxygen electrochemical reactions, which limits its performance in MAB systems. Previous studies have shown that incorporating small amounts of Ag can significantly improve charge-transfer kinetics and ORR activity by providing conductive pathways and synergistic catalytic sites.[14-15] In addition, Ag incorporation can modulate the Mn valence distribution and promote the formation of oxygen vacancies, thereby increasing the density of electrochemically active sites and facilitating oxygen adsorption and redox reactions. Such electronic and structural tuning leads to enhanced bifunctional ORR/OER performance and improved durability of MnO_2-based air cathodes. Therefore, Ag doping represents a rational strategy to overcome the intrinsic limitations of MnO_2 while maintaining low noble-metal loading and achieving improved MABs electrochemical performance.[16-21]

Most previously reported Ag-modified MnO_2 air cathodes have been fabricated as slurry-based composite electrodes relying on polymeric binders and conductive additives to ensure mechanical integrity and electrical connectivity. However, the presence of binders can partially block active sites, hinder mass transport, and compromise long-term stability, particularly under high-rate operation. In contrast, the present work employs a binder-free architecture directly grown on carbon paper, which improves electrical contact and facilitates reactant diffusion, enabling a more reliable evaluation of intrinsic bifunctional electrocatalytic behavior under practical Zn–air battery conditions. This design, combined with controlled Ag incorporation, further allows us to establish a clear composition–performance relationship and identify the optimal balance between conductivity enhancement and preservation of MnO_2 redox-active sites. In this work, we address these limitations by developing binderless MnO_2–Ag air electrodes directly grown on conductive

View Article Online
DOI: 10.1039/D6MA00390G

carbon paper (CP) substrate, thereby maximizing electrical contact and fully exposing the active surface. Notably, Ag incorporation is controlled through ultra-low precursor molar ratios ($Ag/KMnO_4$ = 0.03 and 0.05), allowing us to finely tune the amount of Ag introduced into the MnO_2 matrix while minimizing noble metal usage. This approach enables a clear assessment of the intrinsic synergistic effects of trace Ag incorporation on power performance, and cycling durability in rechargeable Zn–air batteries.

2. Experimental section

2.1. Synthesis of Ag-doped CP/MnO_x

The CP/MnO_x samples were prepared by a simple HT method and a following annealing treatment, which was similar to our previous paper.[22] As to the Ag-doped CP/MnO_x, typically, $KMnO_4$ (0.09 mol L^{-1}) aqueous solution with a volume of about 16.7 mL was thoroughly mixed with silver sulfate (Ag_2SO_4) in concentration tailored to each sample. This was followed by the addition of 0.374 mL concentrated hydrochloric (HCl) acid. The resulting solution was stirred with a magnetic stirrer for 20 minutes and subsequently transferred to an autoclave reactor, which was pre-placed with a piece of CP substrate. Then the reactor went through an HT reaction at 140 °C for 12 h. After the HT process, the on-substrate sample was carefully taken out and washed with ultrapure deionized water (Millipore Milli-Q, resistivity 18.2 MΩ·cm) several times, and annealed at 300 °C for 1 h in air. The Ag content was optimized from the molar ratio of $Ag_2SO_4/KMnO_4$ from 0.03 to 0.05, which were denoted as CP/$MnO_xAg_{0.03}$ and CP/$MnO_xAg_{0.05}$.

2.2. Characterizations

Surface morphology analysis was conducted using a TESCAN VEGA3 scanning electron microscope (SEM) operating at 20 kV. The SEM was equipped with a Quantax detector (Bruker) for energy dispersive X-ray spectroscopy (EDS) mapping and concentration analysis. The crystal structure was examined using a PANalytical AERIS diffractometer (XRD), featuring a Cu Kα source with a step size of 0.0027 degree. Micro-Raman spectroscopy was used for further confirmation of the structural quality with a Renishaw (inVia Reflex) spectroscopy system. A 532 nm laser was applied with a laser power as low as 0.1 mW (1% × 10 mW). Each spectrum was recorded in the Raman shift range of 0-3000 cm^{-1} with a 2 μm spot size and 50 s acquisition time with 3 times acquisition. XPS spectra were recorded with an XPS/HAXPES (PHI Quantes) spectrometer with a traditional soft Al Kα source (1486.6 eV) as an excitation source. Survey

View Article Online
DOI: 10.1039/D6MA00390G

spectra were gathered with high pass energy (280 eV) in the binding energy range of 0-1350 eV to get a preliminary judgment of surface elements; then the core-level spectra of C 1s, O 1s, Mn 2p, Mn 3s, and Ag 3d were collected with lower pass energy (55 eV). All the spectra were interpreted with the CasaXPS software. The high-resolution C 1s spectra of hydrocarbon components at 284.6 eV were used as an internal reference to calibrate the binding energy of all the XPS spectra. The FT-IR spectra of all samples were analyzed using Thermo Scientific 4700 unit.

2.3. Electrochemical measurements-rechargeable Zn-air batteries test

A homemade Zn-air battery model was used to evaluate the Ag-doped on-substrate cathode samples. To prevent the electrolyte leakage problem, one piece of superhydrophobic Toray CP (TGP-H-090) of the same size as our cathode sample was placed together with Ag-doped MnO_x cathode but towards the air side. The effective area of the cathode was 1 cm^2. A piece of Zn plate (0.38 mm in thickness) was used as the Zn anode and the current collector. The current collector on the cathode side was a piece of stainless steel (SS) mesh, and a piece of filter paper served as the separator. The electrolyte was 6.0 M KOH + 0.2 M zinc acetate solution.

The battery test was conducted with an electrochemical workstation (Autolab PGSTAT302). The voltage cut-off values of the battery for the discharging and charging process were 0.6 and 3.0 V, respectively. Firstly, discharge and charge polarization profiles were collected with a low current scan rate (10^{-4} A s^{-1}). The specific capacity of the battery was evaluated by a full-discharging experiment at a current density of 2 mA cm^{-2}. The galvanostatic discharge and charge (GCD) cycling test based on Ag-doped CP/MnO_x cathodes was performed at the current density of 2 mA cm^{-2} for 300 cycles with 20 min for each pulse cycling (10 min discharging and 10 min charging). Electrochemical impedance spectroscopy (EIS) measurements were carried out at the open-circuit potential (OCP) before and after GCD cycling using an Eco Chemie PGSTAT302 potentiostat/galvanostat equipped with the FRA32 module. The spectra were recorded over a frequency range from 100 kHz to 0.1 Hz with an AC perturbation amplitude of 5 mV. All measurements were performed at ambient temperature.

3. Results and discussion

3.1. Morphological and structural characterizations

View Article Online
DOI: 10.1039/D6MA00390G

SEM observations at progressively higher magnifications reveal noticeable morphological differences between $MnO_xAg_{0.03}$ and $MnO_xAg_{0.05}$ (Fig. 1). At low magnification (50 μm scale), both samples uniformly cover the carbon fibers; however, $MnO_xAg_{0.03}$ forms a more continuous and homogeneous coating, whereas $MnO_xAg_{0.05}$ exhibits more localized agglomerates decorating the fiber surfaces. At intermediate magnification (20 μm scale), $MnO_xAg_{0.03}$ shows a sponge-like, finely textured layer composed of densely distributed nanoscale features, indicating a high nucleation density and controlled growth. In contrast, $MnO_xAg_{0.05}$ displays star-like clustered domains and partial coalescence of particles, suggesting enhanced secondary growth and surface roughening at higher Ag content. At high magnification (2 μm scale), both materials consist of MnO_2 nanoneedles, but $MnO_xAg_{0.03}$ presents shorter, densely packed, and randomly oriented needles forming a compact interconnected network, while $MnO_xAg_{0.05}$ shows relatively longer and more distinct nanorods with slightly lower packing density and larger inter-rod spacing. Overall, increasing the Ag content from 0.03 to 0.05 promotes anisotropic crystal growth and aggregation, leading to a transition from a homogeneous nanoneedle network to a coarser, more heterogeneous architecture. The EDX spectra of the Ag-doped MnO_2 samples display only the characteristic signals of C, O, Mn, and K, while no distinct Ag peak is observed (Fig. S1). This apparent absence of Ag is mainly attributed to the extremely low Ag loading, which is below the typical detection limit of conventional SEM–EDX. In addition, the most intense Ag emission lines accessible under common SEM accelerating voltages are the Ag Lα and Lβ peaks located at ~2.98 and ~3.15 keV, respectively. These energies are very close to the strong K Kα peak (~3.31 keV) arising from residual K^+ ions in the α-MnO_2 tunnel structure, leading to significant spectral overlap and masking of the weak Ag signal.

View Article Online
DOI: 10.1039/D6MA00390G

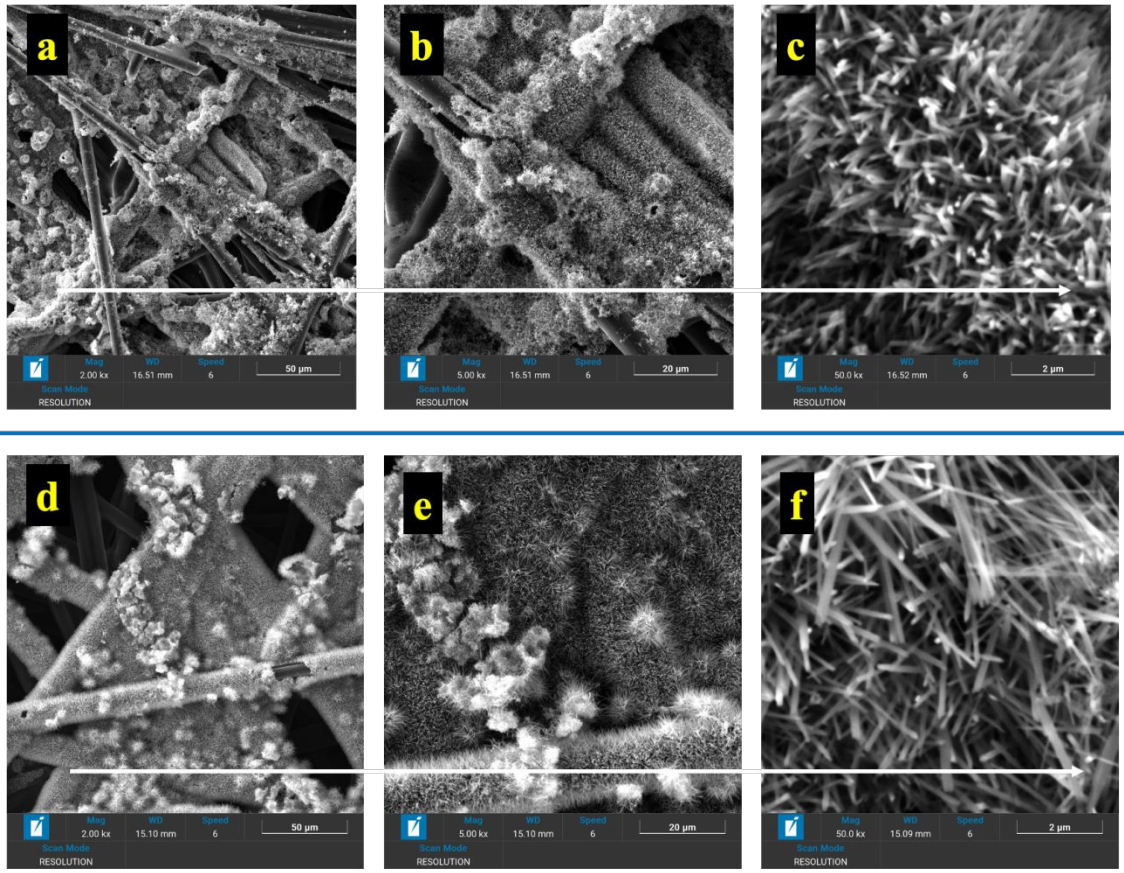

Fig. 1 SEM images of Ag-doped MnO_x grown on carbon paper at increasing magnifications: (a–c) $MnO_xAg_{0.03}$ and (d–f) $MnO_xAg_{0.05}$, showing the overall coverage of the carbon fiber substrate and the evolution of the deposited material with increasing magnification.

The XRD patterns of CP, CP/MnO_x, CP/$MnO_xAg_{0.03}$, and CP/$MnO_xAg_{0.05}$ reveal the structural evolution upon MnO_x deposition and Ag incorporation (Fig. 2a). The pristine carbon paper (CP) exhibits a broad reflection centered at ~26°, which is assigned to the (002) plane of graphitic carbon, corresponding to the interlayer stacking of graphene sheets. After MnO_x growth, additional diffraction peaks emerge at approximately 28°, 37°, 42°, 49°, and 60°, which can be indexed to the (310), (211), (301), (411), and (521) planes of the cryptomelane KMn_8O_{16} (JCPDS 29-1020), a typical tetragonal α-MnO_2 phase in the manganese oxide family, in which K^+ is located in its 2 × 2 tunnels for stabilization of the α phase crystalline structure and charge balance. The relatively broad and low-intensity MnO_2 reflections suggest a nanocrystalline and poorly ordered structure, consistent with the hydrothermal growth of MnO_2 nanoneedles. Upon Ag incorporation (CP/$MnO_xAg_{0.03}$ and CP/$MnO_xAg_{0.05}$), the diffraction patterns remain essentially unchanged, with

View Article Online
DOI: 10.1039/D6MA00390G

no detectable peaks attributable to metallic Ag or silver oxides. The absence of distinct Ag-related diffraction peaks in the XRD patterns suggests that Ag is either highly dispersed, present at low concentration, or exists in an amorphous form. This interpretation is further supported by complementary spectroscopic analyses (Raman and XPS, discussed below), which confirm the presence of Ag and its interaction with the MnO_2 matrix. To further evaluate the structural impact of Ag incorporation, the crystallite size of MnO_2 was estimated using the Scherrer equation. The calculated values increase from 1.30 nm for pristine MnO_2 to 1.77 nm for $MnO_2Ag_{0.03}$, followed by a slight decrease to 1.63 nm for $MnO_2Ag_{0.05}$. This trend indicates that moderate Ag incorporation promotes partial structural ordering or crystallite growth, whereas excessive Ag loading introduces structural disorder. Such evolution in crystallinity is consistent with the electrochemical results, where the optimally doped $MnO_2Ag_{0.03}$ exhibits improved catalytic reversibility and cycling stability, highlighting the critical role of controlled Ag dispersion in tuning the structure–performance relationship.

The FTIR spectra of CP, CP/MnO_x, CP/$MnO_xAg_{0.03}$, and CP/$MnO_xAg_{0.05}$ are shown in Fig. 2b. The pristine carbon paper exhibits bands at ~1201 and ~1147 cm^{-1}, which are attributed to C–O and C–O–C stretching vibrations associated with oxygen-containing functional groups on the carbon surface.[23] These groups can facilitate the nucleation and anchoring of MnO_x during hydrothermal growth. After MnO_2 deposition, a new absorption band appears around ~698 cm^{-1}, corresponding to the Mn–O stretching vibration of MnO_6 octahedra, characteristic of manganese oxide structures.[24] The presence of this band confirms the successful formation of MnO_2 on the carbon paper substrate, in agreement with the XRD and Raman analyses. The overall spectral features remain similar after Ag incorporation, indicating that the MnO_x framework is preserved.

Figure 2c shows the Raman spectra of undoped CP/MnO_x and Ag-doped CP/$MnO_xAg_{0.03}$ and CP/$MnO_xAg_{0.05}$ electrodes. The Raman spectrum of the undoped CP/MnO_x sample exhibits four characteristic bands located at approximately 187, 393, 521, and 640 cm^{-1}, which are well-assigned to tetragonal α-MnO_2, in good agreement with previous reports.[25-26] The intense band at ~640 cm^{-1} corresponds to the A_g symmetric stretching vibration of the Mn–O bond perpendicular to the double chains of edge-sharing [MnO_6] octahedra, while the band at ~521 cm^{-1}, also an A_g mode, is associated with Mn–O stretching along the octahedral chain direction.[25-26] The feature at ~393 cm^{-1} arises from the E_g bending vibration of Mn–O bonds, whereas the sharp low-frequency

View Article Online
DOI: 10.1039/D6MA00390G

peak at ~187 cm^{-1} (E_g mode) is attributed to the translational motion of [MnO_6] octahedra induced by tunnel-stabilizing K^+ ions, a hallmark of well-ordered α-MnO_2 tunnel structures.[27-28]

Upon Ag incorporation, noticeable changes occur in both peak positions and spectral features. A systematic red shift (toward lower wavenumbers) is observed for the principal Mn–O vibrational modes, with the ~640 cm^{-1} band shifting to ~633 cm^{-1}, the ~585 cm^{-1} shoulder to ~572–571 cm^{-1}, and the ~521 cm^{-1} mode to ~492–493 cm^{-1} for the Ag-doped samples. Such red shifts are commonly associated with lattice distortion, bond weakening, or increased structural disorder, which may originate from Ag incorporation at or near the MnO_2 lattice, modification of local Mn–O bond lengths, or the generation of oxygen vacancies to maintain charge balance. Notably, the disappearance of the ~187 cm^{-1} E_g mode in the Ag-doped samples suggests a modification or weakening of the long-range tunnel ordering, as well as changes in the tunnel ion environment. This behavior may be associated with partial substitution or displacement of K^+ ions and an increase in defect density within the α-MnO_2 framework. This interpretation is consistent with the crystallite size evolution derived from XRD analysis, indicating changes in structural ordering upon Ag incorporation. Overall, these observations suggest that Ag doping induces local structural perturbations while preserving the overall α-MnO_2 phase.

View Article Online
DOI: 10.1039/D6MA00390G

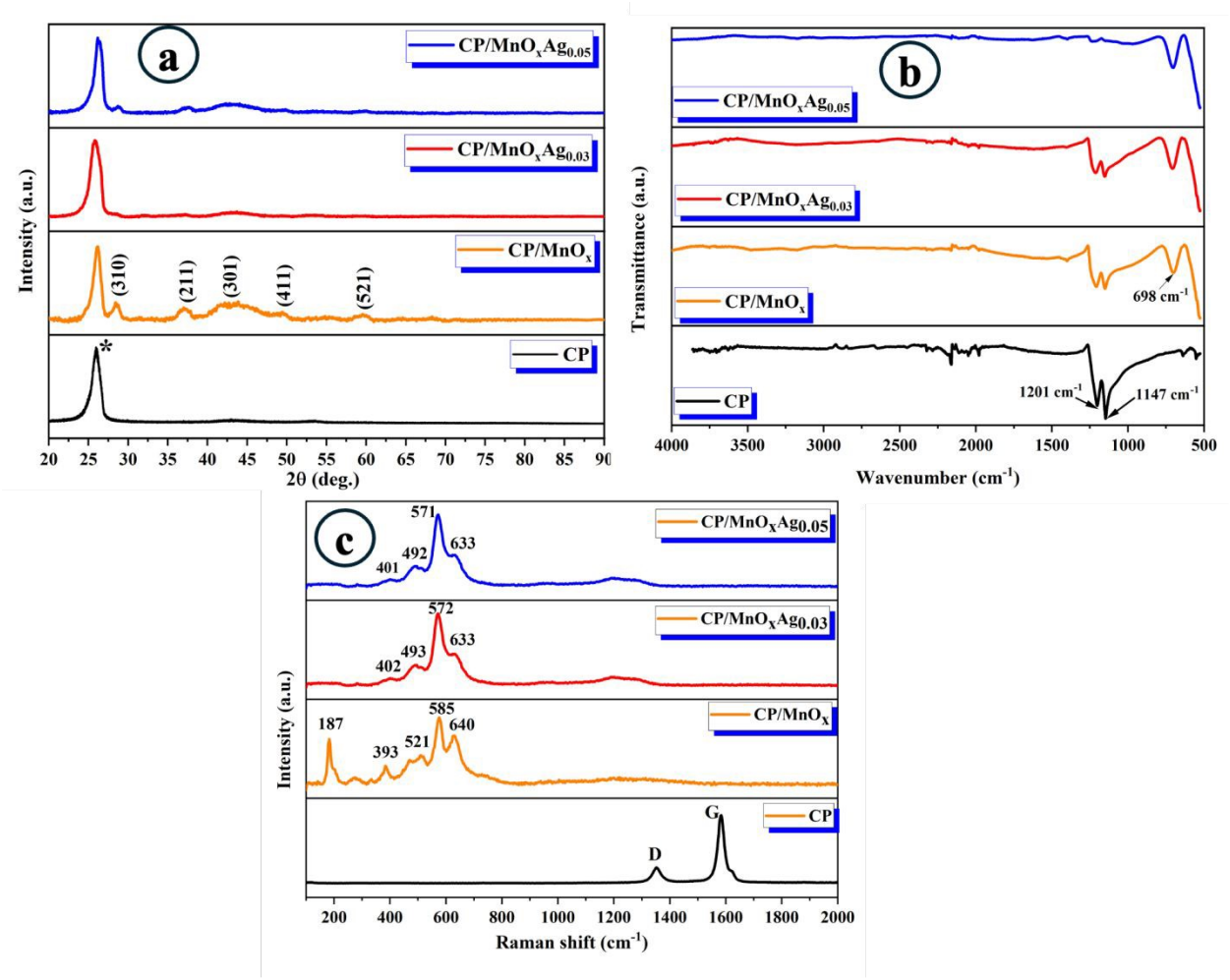

Fig. 2 (a) XRD patterns. (*) correspond to the patterns of the CP substrate. (b) FTIR spectra and (c) Raman spectra of CP/MnO_x, $CP/MnO_xAg_{0.03}$ and $CP/MnO_xAg_{0.05}$, as indicated on the figures.

XPS survey spectrum shown in Fig. S2. The surface chemical states of the Ag-doped MnO_x samples were investigated by XPS through Ag 3d, Mn 2p, and O 1s spectra (Fig. 3). The Ag 3d spectra display two well-defined peaks at binding energies of ~368 and ~374 eV, assigned to Ag $3d_{5/2}$ and Ag $3d_{3/2}$, respectively. The spin–orbit splitting of ~5.93–6.0 eV is widely reported as characteristic of metallic Ag^0, indicating that Ag is predominantly present in metallic form rather than as a separate Ag oxide phase,[29] while still interacting electronically with the MnO_2 matrix. The Mn 2p spectra were deconvoluted into Mn^{4+}, Mn^{3+}, and Mn^{2+} contributions along with a shake-up satellite, revealing a mixed-valence manganese oxide structure. For the Ag-doped samples, quantitative analysis shows Mn^{3+} as the dominant oxidation state (~44–47%), followed by Mn^{4+} (~23–27%) and a smaller Mn^{2+} fraction (~16–18%). In contrast, the non-doped MnO_x

View Article Online
DOI: 10.1039/D6MA00390G

exhibited a markedly different distribution, with Mn^{4+} (~55.2%) as the predominant species, along with Mn^{3+} (~24.4%) and Mn^{2+} (~20.4%).[30] The significant increase in Mn^{3+} content accompanied by the decrease in Mn^{4+} upon Ag incorporation indicates partial reduction of Mn^{4+} to Mn^{3+} and the generation of oxygen vacancies to maintain charge neutrality. This defect-rich environment is consistent with the Raman red shifts, reflecting weakened Mn–O bonds and local lattice distortion within the α-MnO_2 framework. The O 1s spectra further corroborate this interpretation. For the undoped MnO_x, the lattice oxygen (O_latt) and adsorbed oxygen (O_ads) fractions were ~64.7% and ~35.3%, respectively, indicating a relatively higher proportion of surface oxygen species.[30] Upon Ag incorporation, the spectra show a dominant lattice oxygen component (O_latt, ~529–530 eV; ≈70–92%) and a reduced high-binding-energy contribution (O_ads, ~531–532 eV) associated with surface hydroxyl groups and vacancy-related oxygen species. Notably, the sample with lower Ag content exhibits a higher proportion of lattice oxygen, implying improved structural ordering and fewer surface defects, in agreement with the more uniform nanoneedle morphology observed by SEM. Overall, XPS confirms that metallic Ag incorporation induces a shift toward a Mn^{3+}-rich, oxygen-vacancy-modified MnO_2 while preserving the α-MnO_2 phase.

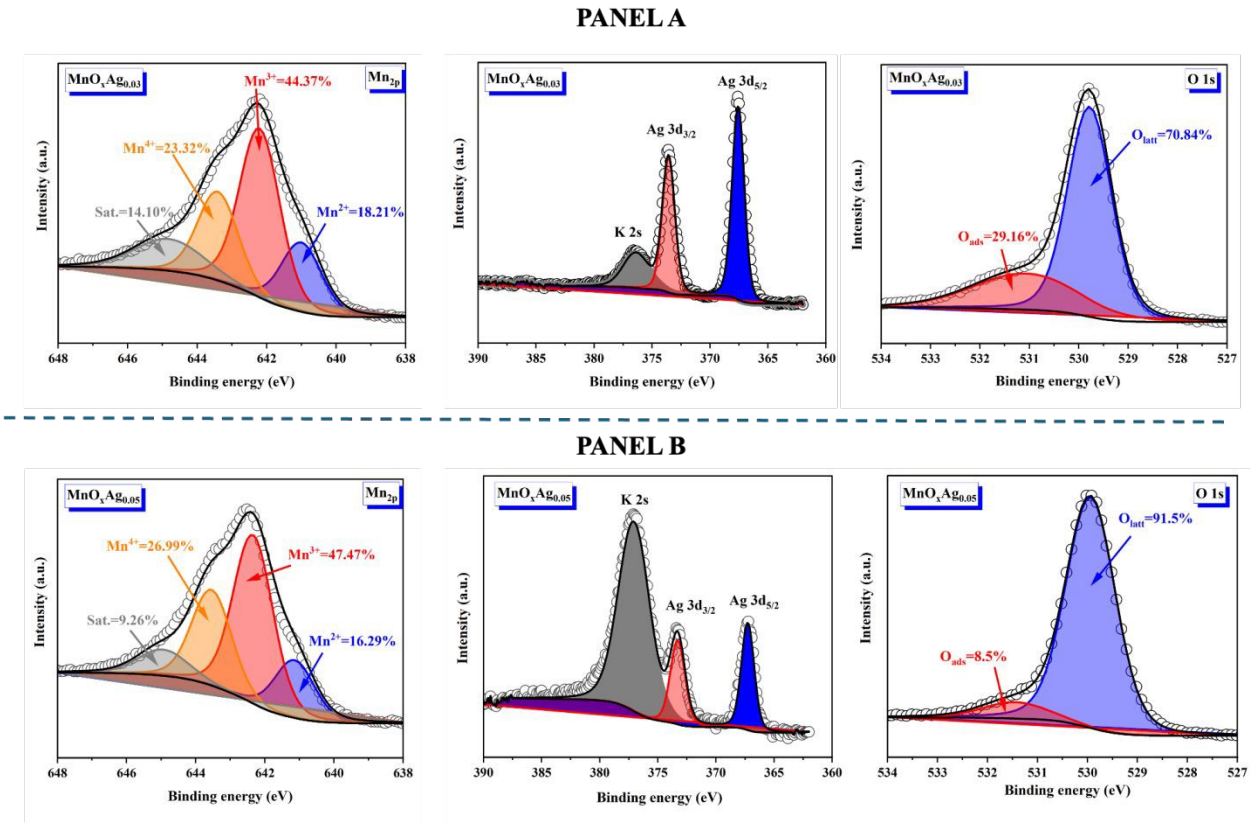

View Article Online
DOI: 10.1039/D6MA00390G

Fig. 3 High-resolution XPS spectra of Ag-doped MnO_x cathodes with different Ag loadings: (PANEL A) $MnO_xAg_{0.03}$ and (PANEL B) $MnO_xAg_{0.05}$. From left to right, the deconvoluted spectra correspond to the Mn 2p, Ag 3d (overlapping with K 2p), and O 1s regions.

Overall, the combined structural and spectroscopic analyses provide a consistent description of the Ag-modified MnO_2 system. SEM observations reveal the formation of dense MnO_2 nanoneedle structures uniformly covering the carbon paper substrate. XRD patterns confirm that the deposited oxide crystallizes in the tetragonal α-MnO_2 phase and that this long-range crystal structure is preserved after Ag incorporation. FTIR spectra further verify the presence of Mn–O bonding without significant modification of the fundamental MnO_2 framework. In contrast, Raman spectroscopy reveals slight red shifts of the Mn–O vibrational modes upon Ag incorporation, suggesting local lattice distortion within the MnO_6 octahedral network. XPS analysis provides further insight by showing an increased Mn^{3+} fraction and the presence of metallic Ag, indicating that Ag incorporation promotes defect formation and oxygen-vacancy generation. These results collectively demonstrate that Ag doping primarily induces short-range structural and electronic modifications while preserving the overall α-MnO_2 framework.

3.2. Electrochemical performance

To elucidate the effect of Ag incorporation on the electrochemical properties of MnO_x, the electrochemical behavior of CP/MnO_x, CP/$MnO_xAg_{0.03}$, and CP/$MnO_xAg_{0.05}$ electrodes was systematically investigated.

Figure 4 shows the discharge voltage and corresponding power density as a function of current density for Zn–air batteries assembled with MnO_x, $MnO_xAg_{0.03}$, and $MnO_xAg_{0.05}$ air cathodes. The undoped MnO_x electrode delivers a maximum current density of 70.9 mA cm^{-2} and a peak power density of 21.9 mW cm^{-2}, reflecting pronounced polarization losses at elevated discharge rates. Introducing Ag markedly alters the discharge behavior. While $MnO_xAg_{0.03}$ achieves a higher maximum current density (80.5 mA cm^{-2}), its peak power density slightly decreases to 18.9 mW cm^{-2}. In contrast, the $MnO_xAg_{0.05}$ air cathode exhibits a substantial enhancement in Zn–air battery performance, delivering a maximum current density of 80.5 mA cm^{-2} and a significantly increased peak power density of 39.1 mW cm^{-2}. This corresponds to a ~78.5% improvement in maximum power density compared to undoped MnO_x and a ~107% increase relative to $MnO_xAg_{0.03}$.

View Article Online
DOI: 10.1039/D6MA00390G

Additionally, $MnO_xAg_{0.05}$ maintains higher discharge voltages over the entire current density range, indicating reduced activation and ohmic polarization. The pronounced improvement at higher Ag content highlights the critical role of Ag in enhancing electronic conductivity and accelerating oxygen reduction reaction kinetics at the air cathode. These results demonstrate that optimized Ag incorporation is essential to fully exploit the catalytic activity of MnO_x and maximize the power output of Zn–air batteries.

This enhancement can be correlated with the XPS analysis by comparison with the undoped MnOx. The pristine MnOx is dominated by Mn^{4+} species (≈55.2%) with a relatively low Mn^{3+} content (≈24.4%), whereas Ag incorporation significantly increases the Mn^{3+} fraction at the expense of Mn^{4+} (Fig. 3). This shift indicates partial reduction of Mn^{4+} and the formation of a more defect-rich structure. Such modification of the Mn valence state is known to enhance electronic conductivity and facilitate oxygen electrocatalysis, thereby improving ORR/OER kinetics. In addition, changes in oxygen species reflect a modified local bonding environment, which can further contribute to catalytic activity. Overall, these results demonstrate that Ag incorporation effectively tunes the electronic structure of MnOx, leading to enhanced bifunctional performance compared to the undoped electrode.

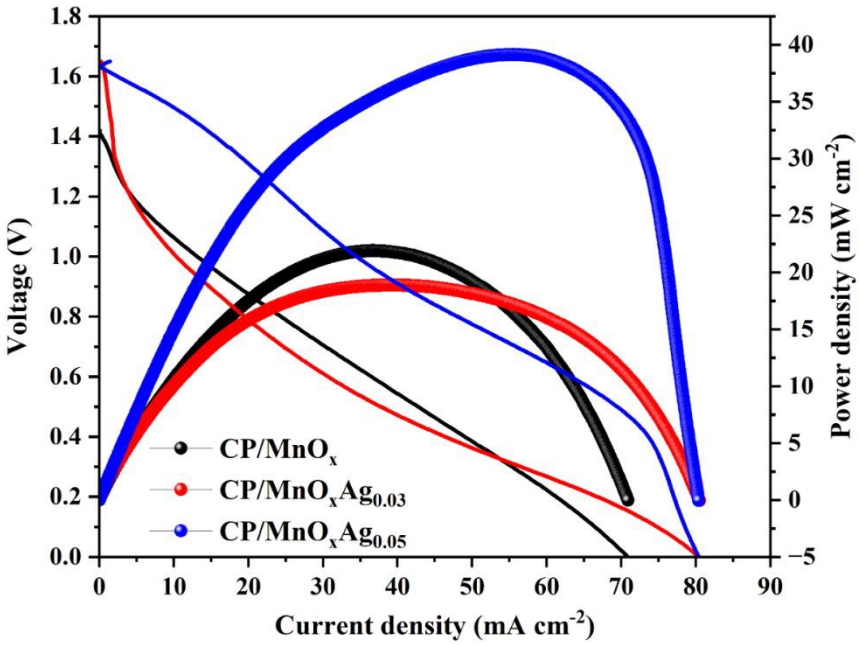

View Article Online
DOI: 10.1039/D6MA00390G

Fig. 4 Polarization and corresponding power density curves of Zn–air batteries employing CP/MnO_x (black), $MnO_xAg_{0.03}$ (red), and $MnO_xAg_{0.05}$ (blue) air cathodes.

Figure 5 presents the galvanostatic charge–discharge cycling profiles of ZABs assembled with undoped CP/MnO_x (Fig. 5a), CP/$MnO_xAg_{0.03}$ (Fig. 5b), and CP/$MnO_xAg_{0.05}$ (Fig. 5c) air cathodes. Long-term cycling tests were conducted over 300 cycles at a current density of 2 mA cm^{-2} with 20 min pulse cycles (10 min discharge and 10 min charge), while short-term profiles over 10 cycles (Fig. 5d–f) highlight voltage hysteresis and reversibility. The CP/$MnO_xAg_{0.03}$-based ZAB exhibits generally stable charge–discharge profiles with only a modest increase in polarization upon prolonged cycling. The short-term curves display reproducible and symmetric plateaus, indicating good reversibility of the oxygen electrochemistry. The CP/$MnO_xAg_{0.05}$ electrode also shows stable and well-defined plateaus, reflecting improved reaction kinetics and enhanced structural robustness of the air cathode. However, quantitative analysis of the voltage gap and round-trip efficiency reveals that CP/$MnO_xAg_{0.03}$ provides the most favorable bifunctional performance during cycling (Fig. 5j-k). At the initial cycle, pristine MnO_x exhibits a large voltage gap of 1.09 V and a low round-trip efficiency (46.5%), indicating sluggish ORR/OER kinetics. Incorporation of a small amount of Ag ($MnO_xAg_{0.03}$) significantly reduces the voltage gap to 0.87 V and increases the efficiency to 59.1%, evidencing enhanced catalytic reversibility. Increasing the Ag loading to 0.05 only slightly decreases the initial gap (0.85 V) but does not further improve the efficiency (55%), suggesting that excessive Ag does not proportionally enhance bifunctional activity.

After 300 cycles, clear differences in durability emerge. Pristine MnO_x undergoes severe degradation, with the voltage gap widening to 1.5 V and the efficiency dropping to 37.5%. CP/$MnO_xAg_{0.03}$ shows the best retention, maintaining a relatively small gap (1.09 V) and a high efficiency of 50.6%, highlighting its superior catalytic stability and balanced ORR/OER kinetics. Although CP/$MnO_xAg_{0.05}$ performs better than bare MnO_x, its gap increases to 1.32 V and the efficiency declines to 40.3%, indicating faster polarization growth compared with CP/$MnO_xAg_{0.03}$. Overall, these results demonstrate that moderate Ag incorporation (0.03) optimizes bifunctional reversibility, while higher loading (0.05) mainly enhances kinetic robustness rather than long-term energy efficiency.

View Article Online
DOI: 10.1039/D6MA00390G

The Nyquist plots recorded before and after 300 charge–discharge cycles provide insight into the evolution of the interfacial kinetics and transport properties of the air cathodes (Fig. 5g-i). For CP/MnO_x, a pronounced enlargement of the semicircle is observed after cycling, indicating a significant increase in charge-transfer resistance due to catalyst degradation and sluggish ORR/OER kinetics. In comparison, CP/$MnO_xAg_{0.03}$ exhibits a moderate increase in low-frequency impedance, suggesting some transport limitations, while maintaining relatively stable interfacial kinetics. Notably, CP/$MnO_xAg_{0.05}$ shows only a slight change in semicircle diameter after cycling, evidencing improved electronic conductivity retention and structural robustness imparted by higher Ag loading. However, despite its lower impedance evolution, $MnO_xAg_{0.05}$ displays a larger voltage gap and lower round-trip efficiency compared to $MnO_xAg_{0.03}$, indicating that minimal charge-transfer resistance alone does not guarantee optimal bifunctional reversibility. Instead, the results suggest that moderate Ag incorporation (0.03) better preserves the balance between ORR and OER kinetics during prolonged cycling, while higher Ag loading primarily enhances conductivity and instantaneous reaction rates.

The fitted impedance parameters are summarized in Table S1. Because different equivalent circuits are required to accurately describe each system, the extracted parameters are interpreted in terms of qualitative trends rather than direct numerical comparison. The spectra of CP/MnOx and CP/MnOx$Ag_{0.05}$ are well fitted using a two-time-constant model, $R_s(R_1Q_1)(R_1Q_1)$, where the high-frequency component (R_1Q_1) is associated with charge-transfer processes and the low-frequency component (R_2Q_2) reflects mass transport limitations and interfacial heterogeneity. In contrast, the CP/MnOx$Ag_{0.03}$ electrode is adequately described by a simplified $R_s(RQ)$ circuit, indicating that these contributions are not resolved as distinct processes but instead manifest as a single dominant time constant. This behavior points to a more homogeneous electrochemical interface, where charge transfer and transport processes are efficiently coupled.

The reappearance of a second time constant for MnOx$Ag_{0.05}$ after cycling suggests increased interfacial heterogeneity and the development of transport limitations, consistent with post-cycling SEM observations (shown below) showing pronounced structural coarsening. Overall, these results demonstrate that optimal Ag incorporation enhances not only conductivity but also interfacial uniformity and durability, whereas excessive Ag loading leads to performance deterioration despite improved electronic pathways.

View Article Online
DOI: 10.1039/D6MA00390G

Peak power density evaluates discharge capability, whereas round-trip efficiency and voltage gap are more representative metrics for rechargeable Zn–air battery operation. Although $MnO_xAg_{0.05}$ delivers the highest peak power density due to enhanced electronic conductivity and faster ORR kinetics, $MnO_xAg_{0.03}$ exhibits superior round-trip efficiency and lower voltage gap during long-term cycling, indicating that balanced bifunctional activity rather than maximum instantaneous power governs rechargeable Zn–air battery performance.

View Article Online
DOI: 10.1039/D6MA00390G

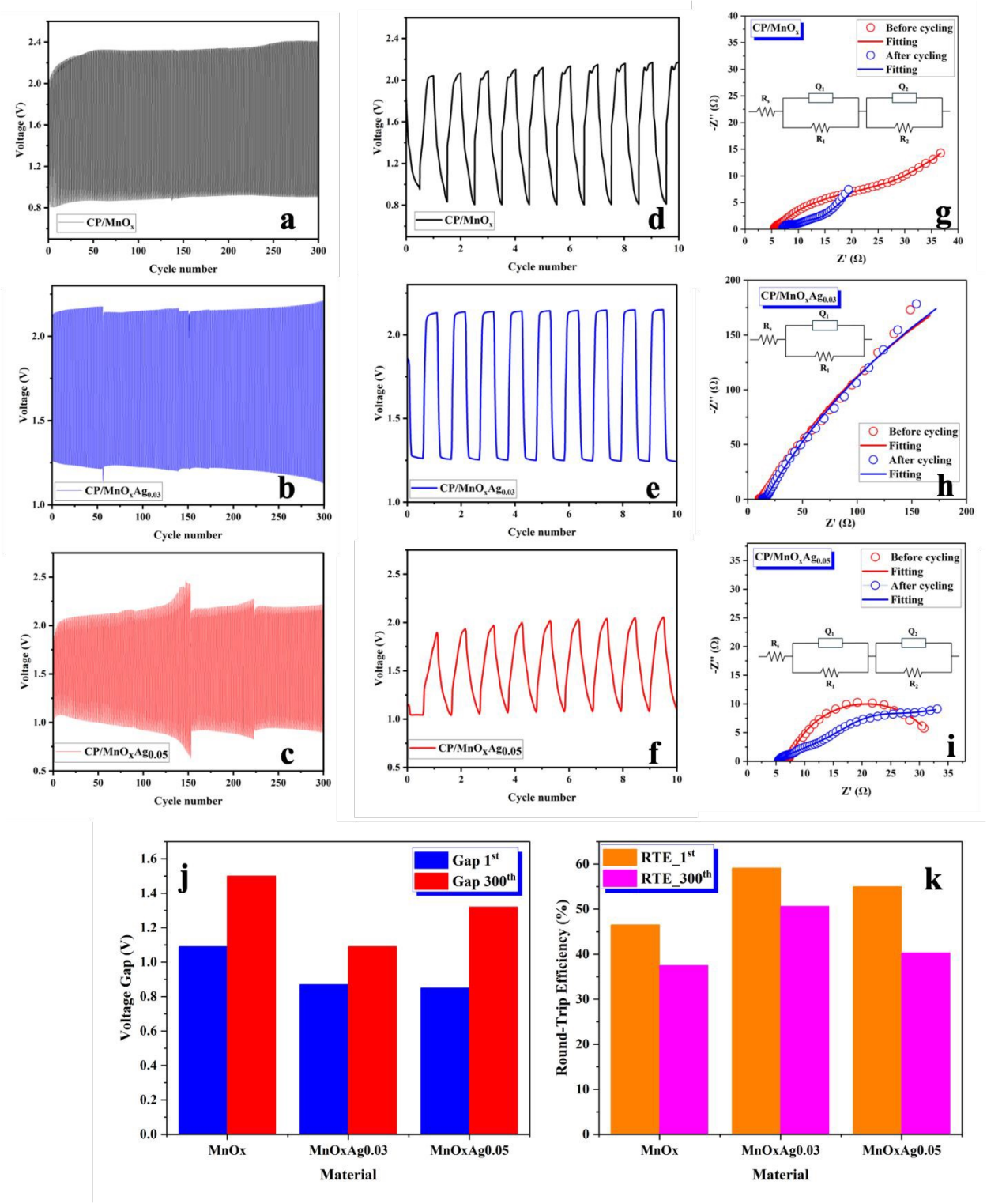

Fig. 5 Galvanostatic charge–discharge cycling profiles of ZABs assembled with (a) undoped CP/MnO_x, (b) $CP/MnO_xAg_{0.03}$, and (c) $CP/MnO_xAg_{0.05}$ air cathodes. Long-term cycling tests were conducted over 300 cycles at a current density of 2 mA cm^{-2} with 20 min pulse cycles (10 min

View Article Online
DOI: 10.1039/D6MA00390G

discharge and 10 min charge), while short-term profiles over 10 cycles (d–f). (g-i) EIS spectra before and after 300 cycles of charge-discharge. (j-k) Comparison of performance of MnO_x, $MnO_xAg_{0.03}$ and $MnO_xAg_{0.05}$ in Zn–air batteries: (j) voltage gap between charge and discharge at the 1st and 300th cycles; (k) corresponding round-trip efficiency (RTE), highlighting the optimal activity–stability balance for CP/$MnO_xAg_{0.03}$.

To gain insight into the degradation mechanisms, post-cycling SEM analysis was performed on the electrodes after 300 charge–discharge cycles (Figure 6). Significant differences in morphological evolution are observed among the samples. The pristine CP/MnO_x electrode exhibits noticeable structural degradation, with partial collapse of the nanostructured features and reduced surface roughness, indicating poor structural stability during cycling. In contrast, the CP/$MnO_xAg_{0.03}$ electrode largely preserves its initial nanowire-like architecture, maintaining a porous and interconnected structure even after prolonged operation. This morphological stability suggests that moderate Ag incorporation effectively stabilizes the MnO_x framework, likely by enhancing electronic conductivity and mitigating structural degradation during repeated ORR/OER processes. On the other hand, the CP/$MnO_xAg_{0.05}$ electrode undergoes pronounced morphological changes, characterized by agglomeration and coarsening of the nanostructures into denser clusters. Such structural evolution leads to a reduction in accessible active surface area and may hinder oxygen diffusion and electrolyte penetration. This degradation is consistent with the observed increase in voltage polarization and decline in round-trip efficiency during cycling.

These results demonstrate that the improved durability of CP/$MnO_xAg_{0.03}$ arises from its ability to maintain structural integrity under operating conditions, whereas excessive Ag loading (0.05) accelerates morphological coarsening and performance decay. This observation highlights the critical role of controlled Ag incorporation in balancing conductivity enhancement and structural stability in MnO_x-based air cathodes.

View Article Online
DOI: 10.1039/D6MA00390G

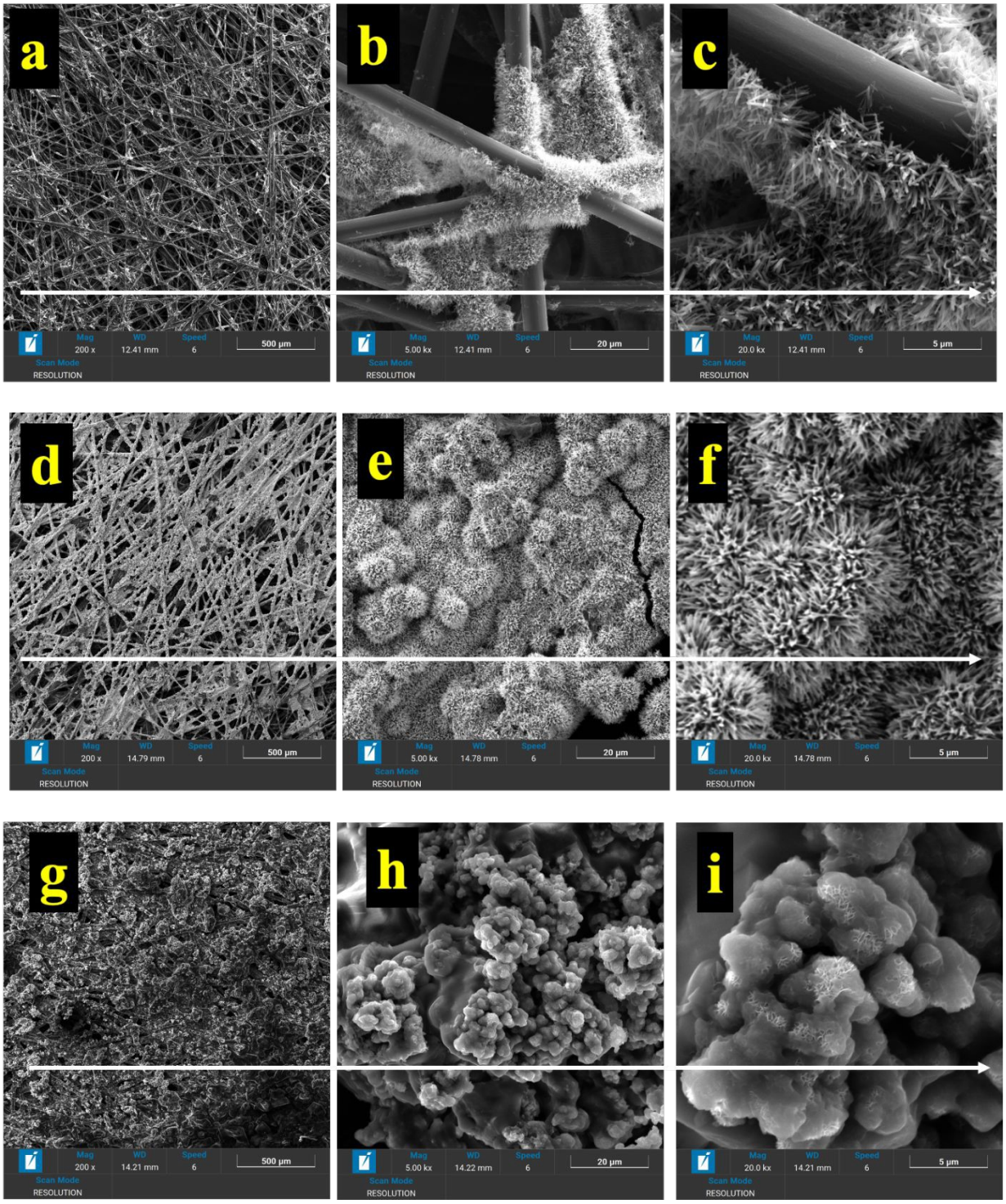

Fig. 6 SEM images of (a–c) CP/MnO_x, (d–f) CP/$MnO_xAg_{0.03}$, and (g–i) CP/$MnO_xAg_{0.05}$ after 300 charge–discharge cycles, showing the morphological evolution and structural stability of the electrodes.

View Article Online
DOI: 10.1039/D6MA00390G

To contextualize the performance of the developed air cathodes, a comparison with representative MnO_2-based and non-precious metal catalysts reported in the literature is provided in Table S2. It is important to note that most reported systems are based on slurry-cast composite electrodes incorporating polymeric binders and conductive additives, whereas the present work employs a binder-free architecture directly grown on carbon paper. Direct comparison should therefore be interpreted with caution, as electrode configuration plays a critical role in determining apparent performance metrics. Despite these differences, the CP/$MnO_2Ag_{0.03}$ electrode demonstrates competitive performance, particularly in terms of voltage gap (1.09 V after 300 cycles) and round-trip efficiency (50.6%), which are comparable to or better than many MnO_2-based systems reported in the literature. While higher power densities are achieved in some composite electrodes, these often rely on additional conductive additives and optimized architectures. In contrast, the binder-free configuration used here enables a more direct assessment of intrinsic catalytic behavior and highlights the importance of composition control. The results clearly demonstrate that moderate Ag incorporation provides an optimal balance between conductivity enhancement and preservation of MnO_2 redox-active sites, leading to improved long-term bifunctional performance.

4. Conclusion

This work demonstrates that controlled Ag incorporation into MnO_x air cathodes plays a decisive role in governing the balance between instantaneous power output and long-term bifunctional reversibility in rechargeable Zn–air batteries. While increasing the Ag loading enhances electronic conductivity and facilitates faster ORR kinetics, the overall rechargeable performance is strongly dependent on achieving an optimal Ag content that preserves the intrinsic Mn redox-active sites responsible for reversible oxygen electrocatalysis.

Electrochemical polarization and power density measurements reveal that $MnO_xAg_{0.05}$ delivers the highest current and power density, highlighting the beneficial role of Ag in improving charge-transfer kinetics and conductive pathways within the air electrode. However, galvanostatic cycling tests demonstrate that $MnO_xAg_{0.03}$ exhibits the lowest voltage gap and the highest round-trip efficiency over 300 cycles, indicating superior bifunctional catalytic reversibility and durability. This result shows that maximizing peak power output does not necessarily translate into optimal rechargeable battery performance.

View Article Online
DOI: 10.1039/D6MA00390G

Impedance spectroscopy further corroborates these findings by revealing distinct stability mechanisms depending on Ag content. After prolonged cycling, $MnO_xAg_{0.05}$ maintains relatively low charge-transfer resistance, evidencing improved electrical stability, whereas $MnO_xAg_{0.03}$ shows a moderate increase in low-frequency impedance but preserves more balanced ORR/OER kinetics. In contrast, undoped MnO_x undergoes significant impedance growth, reflecting severe catalytic degradation and sluggish interfacial kinetics.

Overall, the results establish that an optimal moderate Ag loading (0.03) provides the best compromise between electronic conductivity, catalytic reversibility, and structural stability, leading to enhanced long-term rechargeable performance of Zn–air batteries. Excessive Ag incorporation (0.05), although beneficial for instantaneous power delivery, partially disrupts the ORR/OER kinetic balance and accelerates polarization growth during cycling. These findings highlight the critical importance of tuning metal loading to simultaneously optimize conductivity and preserve active MnO_x redox centers, providing a clear design guideline for developing efficient and durable bifunctional air cathodes for rechargeable Zn–air energy storage systems.

Conflicts of interest

"There are no conflicts to declare".

Data availability

Data will be made available on request.

Acknowledgement

The authors acknowledge the support the financial support provided by the Natural Sciences Engineering Research Council of Canada (NSERC), the Quebec Centre for Advanced Materials (QCAM) and the Directorate General for Scientific Research and Technological Development (DGRSDT-Algeria). We are grateful for Christophe Chabanier at INRS-EMT, for the training and assistance on XPS characterizations.

View Article Online
DOI: 10.1039/D6MA00390G

References

1. M. Barman, M. Pal, R. Biswas and A. Dutta, *Catal. Today*, **2025**, *451*, 115229. https://doi.org/10.1016/j.cattod.2025.115229.
2. T. Li, M. Huang, X. Bai and Y.-X. Wang, *Prog. Nat. Sci.: Mater. Int.*, **2023**, *33*, 151–171. https://doi.org/10.1016/j.pnsc.2023.05.007.
3. A. G. Olabi, E. T. Sayed, T. Wilberforce, A. Jamal, A. H. Alami, K. Elsaid, S. M. A. Rahman, S. K. Shah and M. A. Abdelkareem, *Energies*, **2021**, *14*, 7373. https://doi.org/10.3390/en14217373.
4. P. E. Olli and T. Romann, *J. Chem. Educ.*, **2023**, *100*, 259–266. https://doi.org/10.1021/acs.jchemed.2c00994.
5. Y. Ran, C. Xu, D. Ji *et al.*, *Nano Res. Energy*, **2024**, *3*, e9120092. https://doi.org/10.26599/NRE.2023.9120092.
6. J. Wang, C.-X. Zhao, J.-N. Liu, D. Ren, X. Ma, B.-Q. Li, J.-Q. Huang and Q. Zhang, *Particuology*, **2023**, *77*, 146–152. https://doi.org/10.1016/j.partic.2022.09.003.
7. J. Sun, N. Wang, Z. Qiu, L. Xing and L. Du, *Catalysts*, **2022**, *12*, 843. https://doi.org/10.3390/catal12080843.
8. Y. Li and J. Lu, *ACS Energy Lett.*, **2017**, *2*, 1370–1377. https://doi.org/10.1021/acsenergylett.7b00119.
9. J. F. Parker, C. N. Chervin, I. R. Pala, M. Machler, M. F. Burz, J. W. Long and D. R. Rolison, *Science*, **2017**, *356*, 415–418. https://doi.org/10.1126/science.aak9991.
10. F. Cheng and J. Chen, *Chem. Soc. Rev.*, **2012**, *41*, 2172–2192. https://doi.org/10.1039/C1CS15228A.
11. K. Zhang, X. Han, Z. Hu, X. Zhang, Z. Tao and J. Chen, *Chem. Soc. Rev.*, **2015**, *44*, 699–728. https://doi.org/10.1039/C4CS00218K.
12. M. Rittiruam, N. Aumnongpho, T. Saelee, P. Khajondetchairit, S. Kheawhom, B. Alling, S. Praserthdam, A. Ektarawong and P. Praserthdam, *J. Energy Storage*, **2024**, *78*, 110005. https://doi.org/10.1016/j.est.2023.110005.
13. M. U. Khalid, S. Zulfiqar, M. N. Khan, I. Shakir, M. F. Warsi and E. W. Cochran, *Mater. Adv.*, **2024**, *5*, 6170–6184. https://doi.org/10.1039/D4MA00118D.
14. H. Huang, Y. Meng, A. Labonte, A. Dobley and S. L. Suib, *J. Phys. Chem. C*, **2013**, *117*, 25352–25359. https://doi.org/10.1021/jp409507h.
15. M. He, Z. Turup, X. Jin and F. Chen, *Int. J. Hydrogen Energy*, **2023**, *48*, 25770–25782. https://doi.org/10.1016/j.ijhydene.2023.03.283.
16. T.-H. Wu, S.-L. Cheng and S.-C. Liao, *Electrochim. Acta*, **2024**, *490*, 144290. https://doi.org/10.1016/j.electacta.2024.144290.
17. S. Sun, H. Miao, Y. Xue, Q. Wang, Q. Zhang, Z. Dong, S. Li, H. Huang and Z. Liu, *J. Electrochem. Soc.*, **2017**, *164*, F768–F774. https://doi.org/10.1149/2.0541707jes.
18. F. W. T. Goh, Z. Liu, X. Ge, Y. Zong, G. Du and T. S. A. Hor, *Electrochim. Acta*, **2013**, *114*, 598–604. https://doi.org/10.1016/j.electacta.2013.10.116.
19. A. K. Worku, D. W. Ayele, N. G. Habtu and M. D. Ambaw, *Heliyon*, **2022**, *8*, e10960. https://doi.org/10.1016/j.heliyon.2022.e10960.
20. G. Zhang and P. Zhang, *Reactions*, **2026**, *7*, 10. https://doi.org/10.3390/reactions7010010.
21. S. Sun, H. Miao, Y. Xue, Q. Wang, S. Li and Z. Liu, *Electrochim. Acta*, **2016**, *214*, 49–55. https://doi.org/10.1016/j.electacta.2016.07.127.

View Article Online
DOI: 10.1039/D6MA00390G

22. S. Bouachma, X. Zheng, A. Moreno Zuria, M. Kechouane, N. Gabouze and M. Mohamedi, *Materials*, **2024**, *17*, 4079. https://doi.org/10.3390/ma17164079.
23. J. L. Figueiredo, M. F. R. Pereira, M. M. A. Freitas and J. J. M. Órfão, *Carbon*, **1999**, *37*, 1379–1389. https://doi.org/10.1016/S0008-6223(98)00333-9.
24. C. M. Julien, M. Massot and C. Poinsignon, *Spectrochim. Acta A*, **2004**, *60*, 689–700. https://doi.org/10.1016/S1386-1425(03)00279-8.
25. C. K. King'ondu, N. Opembe, C.-H. Chen, K. Ngala, H. Huang, A. Iyer, H. F. Garces and S. L. Suib, *Adv. Funct. Mater.*, **2011**, *21*, 312–323. https://doi.org/10.1002/adfm.201001020.
26. F. Wang, J. Deng, S. Impeng, Y. Shen, T. Yan, G. Chen, L. Shi and D. Zhang, *Chem. Eng. J.*, **2020**, *396*, 125192. https://doi.org/10.1016/j.cej.2020.125192.
27. C. Zhu, L. Yang, J. K. Seo, X. Zhang, S. Wang, J. Shin, D. Chao, H. Zhang, Y. S. Meng and H. J. Fan, *Mater. Horiz.*, **2017**, *4*, 415–422. https://doi.org/10.1039/C6MH00556J.
28. T. Gao, M. Glerup, F. Krumeich, R. Nesper, H. Fjellvåg and P. Norby, *J. Phys. Chem. C*, **2008**, *112*, 13134–13140. https://doi.org/10.1021/jp804924f.
29. E. Tzomos, M.-H. Mikkelä, G. Öhrwall, O. Björneholm and M. Tchaplyguine, *Surf. Sci.*, **2023**, *733*, 122307. https://doi.org/10.1016/j.susc.2023.122307.
30. X. Zheng, N. Mohammadi, A. Moreno Zuria and M. Mohamedi, *ACS Appl. Mater. Interfaces*, **2021**, *13*, 61374–61385. https://doi.org/10.1021/acsami.1c22371.

View Article Online
DOI: 10.1039/D6MA00390G

Data availability statements

The data supporting this article have been included as part of the Supplementary Information.